

Article

# Catalytic Oxidation of HCHO over the Sodium-Treated Sepiolite-Supported Rare Earth (La, Eu, Dy, and Tm) Oxide Catalysts

Ning Dong <sup>1</sup>, Qing Ye <sup>1,\*</sup>, Mengyue Chen <sup>1</sup>, Shuiyuan Cheng <sup>1</sup>, Tianfang Kang <sup>1</sup> and Hongxing Dai <sup>2,\*</sup>

<sup>1</sup> Key Laboratory of Beijing on Regional Air Pollution Control, Department of Environmental Science, College of Environmental and Energy Engineering, Beijing University of Technology, Beijing 100124, China; dongning@emails.bjut.edu.cn (N.D.); chenmengyue1125@163.com (M.C.); chengsy@bjut.edu.cn (S.C.); kangtf@bjut.edu.cn (T.K.)

<sup>2</sup> Beijing Key Laboratory for Green Catalysis and Separation, Key Laboratory of Beijing on Regional Air Pollution Control, Laboratory of Catalysis Chemistry and Nanoscience, Department of Chemistry and Chemical Engineering, College of Environmental and Energy Engineering, Beijing University of Technology, Beijing 100124, China

\* Correspondence: yeqing@bjut.edu.cn (Q.Y.); hxdai@bjut.edu.cn (H.D.); Tel.: +86-10-6739-1659 (Q.Y.); +86-10-6739-6118 (H.D.); Fax: +86-10-6739-1983 (Q.Y. & H.D.)

Received: 15 February 2020; Accepted: 10 March 2020; Published: 14 March 2020



**Abstract:** The sodium-treated sepiolite (NaSep)-supported rare earth oxide (RE/NaSep; RE = La, Eu, Dy, and Tm) samples were prepared using the rotary evaporation method. Physicochemical properties of these materials were characterized by XRD, SEM, BET, FTIR, XPS, H<sub>2</sub>-TPR, NH<sub>3</sub>-TPD, and in situ DRIFTS, and their catalytic activities for formaldehyde (HCHO) (2000 ppm) oxidation were evaluated. The results show that loading of the rare earth oxide on NaSep improved its catalytic performance. Among all the samples, Eu/NaSep performed the best, and complete HCHO conversion was achieved at a temperature of 150 °C and a gas hourly space velocity of 240,000 mL/(g h); a good catalytic activity was still maintained after 45 h of stability test. The catalytic oxidation mechanism of HCHO was studied using the in situ DRIFTS technique. As a result, the effective and stable catalytic performance of the Eu/NaSep sample was mainly due to the presence of hydroxyl groups on the sepiolite surface and the doped rare earth oxides, which contributed to its high performance. HCHO oxidation underwent via the steps of HCHO + O<sub>2</sub> → HCOO<sup>-</sup> + OH<sup>-</sup> → H<sub>2</sub>O + CO<sub>2</sub>. It is concluded that the optimal catalytic activity of Eu/NaSep was associated with the highest O<sub>ads</sub>/O<sub>latt</sub> atomic ratio, the largest amount of hydroxyl groups, the highest acidity, and the best reducibility. The present work may provide new insights into the application in the removal of high-concentration HCHO over the rare earth oxides supported on natural low-cost clays.

**Keywords:** sodium-treated sepiolite; rare earth oxide; volatile organic compound; HCHO oxidation

## 1. Introduction

Formaldehyde (HCHO) is a harmful pathogenic gas emitted from decorative materials and ordinary furniture [1]. Prolonged exposure to HCHO may cause various discomforts, diseases, and even cancer. People are easily exposed to HCHO in their daily lives, and a series of diseases and even deaths caused by HCHO pollution have received widespread attention. Therefore, it is particularly necessary to control HCHO pollution, and finding a way to effectively remove formaldehyde is an urgent problem to be solved. At present, many effective methods have been developed for the removal

of HCHO, such as catalytic oxidation [2–4], adsorption [5], and plasma purification [6], among which catalytic oxidation is currently considered to be the most promising and most effective method [7,8].

Since HCHO is widely present and easy to produce, it is a current hot research topic to develop an efficient, low-temperature, and low-cost catalyst for HCHO removal. There are many reports on catalytic oxidation of HCHO to CO<sub>2</sub> and H<sub>2</sub>O. Supported noble metals (e.g., Au, Ag, Pd, and Pt) have the advantages of high activity and good stability. For example, Imamura et al. [9] found that the Ag–Ce composite oxide showed a temperature of less than 150 °C for the total conversion of HCHO. Alvarez et al. [10] reported that 0.4 wt % Pd–Mn/Al<sub>2</sub>O<sub>3</sub> catalyst could completely oxidize HCHO to CO<sub>2</sub> and H<sub>2</sub>O at 90 °C. However, these catalysts are difficult to be widely utilized due to their high cost. Therefore, it is necessary to develop cheap, active, and highly stable catalysts. Loading of rare earth is expected to overcome shortcomings of the supported noble metal catalysts and possess several advantages of lower cost and better thermal stability.

According to the report by Gheorghita et al. [11],  $\gamma$ -Al<sub>2</sub>O<sub>3</sub>-supported rare earth (Y, Dy, Tb, Yb, Ce, Tm, Ho, and Pr) oxides were active for propane oxidative dehydrogenation, and the results showed that propylene selectivity was improved. Zhu et al. [12] synthesized the Au–CeO<sub>2</sub> catalysts for the oxidation of HCHO and observed good activities of the materials at low temperatures.

Sepiolite (Si<sub>12</sub>Mg<sub>8</sub>O<sub>30</sub>(OH)<sub>4</sub>(OH<sub>2</sub>)<sub>4</sub>·8H<sub>2</sub>O) is a natural mineral clay with specific functional groups and fibrous shapes. There are alternating blocks in the direction of the fibers as well as the internal tunnels. The block structure is surrounded by two tetrahedral SiO<sub>2</sub>, and the center is composed of MgO [13], which has the advantages of good plasticity, high temperature resistance, large surface area, and good adsorption behaviors. In fact, sepiolite possesses higher adsorption capacity and better stability than the other silicate clays, and has been used to prepare the emerging catalysts due to its low cost, easy availability, and environmental friendliness. For example, Song et al. [14] studied the oxidation of CO over the Cu–Mn/Ti–Sep catalysts at low temperatures. Ma et al. [15] pointed out that HCHO could completely be converted over the 1 wt % Pt/Sep catalyst at room temperature. Zhang et al. [16] observed that the TiO<sub>2</sub>/Sep catalyst was active for the decomposition of HCHO.

Modification of sepiolite with sodium can improve its thermal stability and cation exchange capacity, but the original structure of sepiolite is not changed. Moreover, the rare earth elements are much cheaper and exhibit better stability than the noble metals. In this work, we used the Na-treated sepiolite (NaSep) as a support to prepare the RE/NaSep (RE = La, Eu, Dy, and Tm) catalysts, and explored their physicochemical properties, catalytic activities, reaction mechanisms, and stability for HCHO (2000 ppm) oxidation at a gas hourly space velocity (GHSV) of 240,000 mL/(g h).

## 2. Results and Discussion

### 2.1. Crystal Structure

XRD patterns of the NaSep and RE/NaSep samples are shown in Figure 1. The diffraction peaks of each sample appeared at  $2\theta = 20.6^\circ, 28.0^\circ, 35.2^\circ, 40.4^\circ, \text{ and } 50.2^\circ$ , which could be attributed to the characteristic XRD signals of the sepiolite [17]. The results indicate that the structure of NaSep was not changed after loading of rare earth oxides. In the RE/NaSep samples, no obvious diffraction peaks of rare earth oxides were observed, indicating that the loaded rare earth oxides were homogeneously dispersed on the surface of NaSep.

FTIR is usually used to analyze the structure of amorphous crystals and short-range ordered materials, which can show the structure of a material more comprehensively. Figure 2 shows the FTIR spectra of the NaSep and RE/NaSep samples. There were absorption bands at 3670, 3580, 3420, 1630, 1040, 680, and 480 cm<sup>-1</sup> for each of the samples. The bands at 3670 and 3580 cm<sup>-1</sup> were assigned to the stretching vibrations of the sepiolite hydroxyl group [18,19]; the ones at 3420 and 1630 cm<sup>-1</sup> were attributed to the tensile and bending vibrations of OH in bound water of the zeolitic and sepiolite nanofibrous structure [20,21]; the ones at 1040 and 480 cm<sup>-1</sup> were caused by the tensile vibration of Si–O in the tetrahedral Si–O–Si group and the bending vibration of Si–O–Si [22], respectively;

and the one at  $680\text{ cm}^{-1}$  was attributable to the bending vibration of  $\text{Mg}_3\text{OH}$  [23]. Compared with characteristic bands of NaSep, those of the RE/NaSep samples did not change significantly, and the loading of rare earth oxides had no effect on the structure of sepiolite, coinciding with the XRD results of the samples.

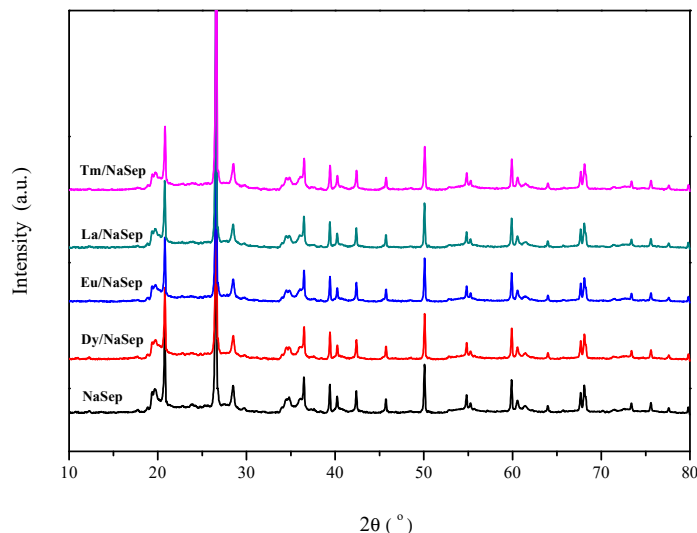


**Figure 1.** XRD patterns of sodium-treated sepiolite (NaSep), Eu/NaSep, Dy/NaSep, La/NaSep, and Tm/NaSep.

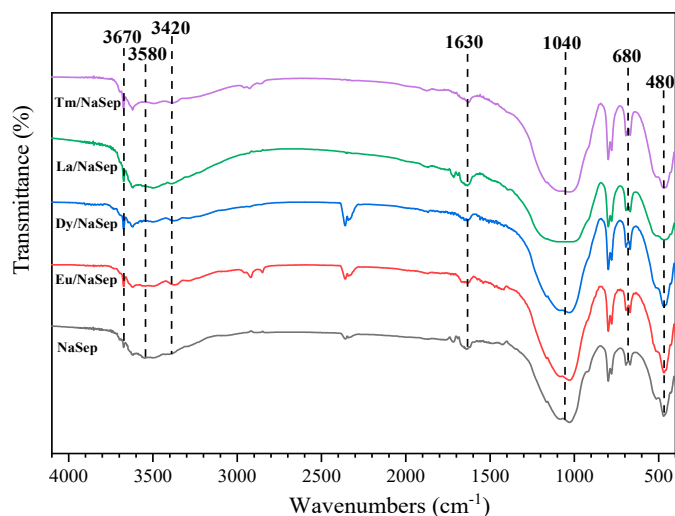


**Figure 2.** FTIR spectra of NaSep, Eu/NaSep, Dy/NaSep, La/NaSep, and Tm/NaSep.

## 2.2. Textural Property and Morphology

Figure 3 shows  $\text{N}_2$  adsorption–desorption isotherms of the NaSep and RE/NaSep samples. The isotherm of each sample corresponded to the type I in the range of low relative pressures, which was due to the existence of a microporous structure [24]. When the relative pressure was in the range of 0.8–1.0, there was a type IV adsorption isotherm with a type H3 hysteresis loop, indicating the presence of the slit-like mesopores [25]. BET surface areas of the NaSep and RE/NaSep samples were listed in Table 1. The surface area of RE/NaSep ( $31\text{--}64\text{ m}^2/\text{g}$ ) was much lower than that ( $96\text{ m}^2/\text{g}$ ) of NaSep, which was due to the fact that the loaded rare earth oxide might partially block the pores of NaSep [26]. Surface area decreased in the order of NaSep ( $96\text{ m}^2/\text{g}$ ) > Tm/NaSep ( $64\text{ m}^2/\text{g}$ ) > La/NaSep ( $47\text{ m}^2/\text{g}$ ) > Eu/NaSep ( $43\text{ m}^2/\text{g}$ ) > Dy/NaSep ( $31\text{ m}^2/\text{g}$ ).

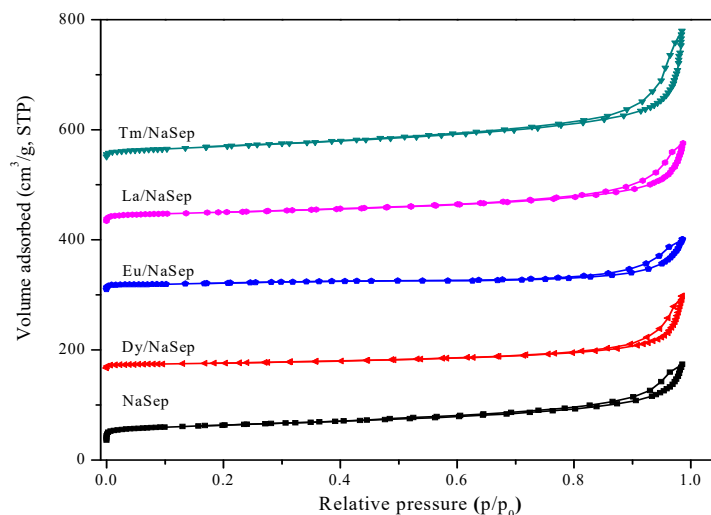


Figure 3.  $N_2$  adsorption–desorption isotherms of the samples.

Table 1. BET surface areas, pore volumes, and pore diameters.

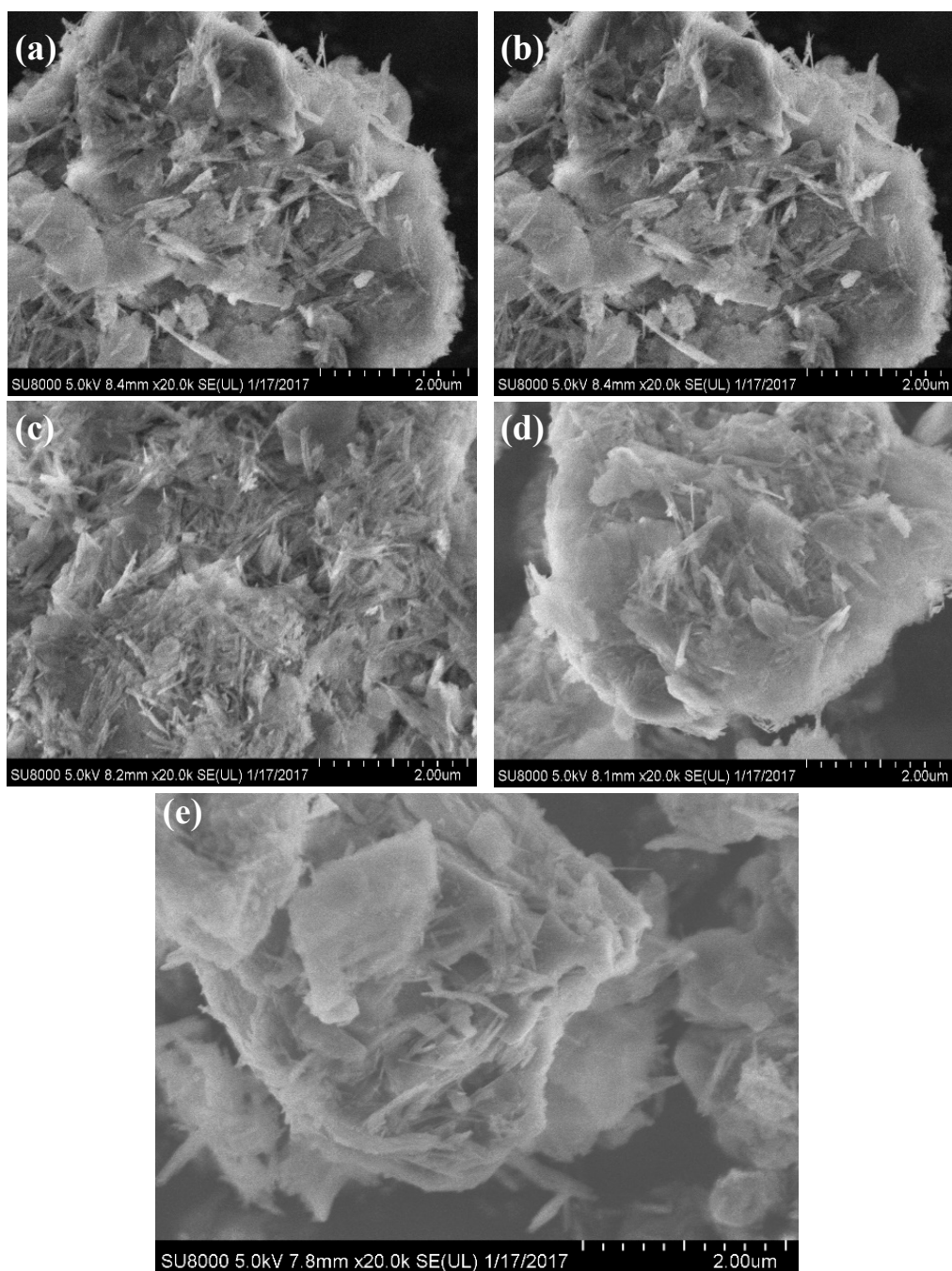
Sample	Surface Area ( $m^2/g$ )	Pore Volume ( $cm^3/g$ )	Pore Diameter (nm)
NaSep	96	0.214	8.9
La/NaSep	47	0.207	17.8
Eu/NaSep	43	0.126	10.7
Dy/NaSep	31	0.203	26.9
Tm/NaSep	64	0.354	24.6

Figure 4 shows the morphologies of the NaSep and RE/NaSep samples. Each sample possessed a fibrous morphology, indicating the formation of a typical sepiolite structure. Although the RE/NaSep samples showed different surface areas, there was no significant morphological difference between RE/NaSep and NaSep, indicating that loading of rare earth oxides did not change the physical structure of sepiolite.

### 2.3. Surface Element Composition and Adsorbed Oxygen Species

XPS was used to analyze surface compositions and chemical states of the samples, and their XPS spectra and surface compositions are presented in Figure 5 and Table 2, respectively. The Dy 4d<sub>5/2</sub> spectrum of the Dy-loaded sample exhibited two components at binding energy (BE) = 153.7 and 155.9 eV, which were assigned to the surface Dy<sup>3+</sup> species [27]. The Eu 4d spectrum of the Eu-loaded sample showed two asymmetric characteristic signals at BE = 141.4 and 135.1 eV, which indicates the presence of surface Eu<sup>3+</sup> species [28]. The main peak at BE = 834.5 eV as well as its satellite at BE = 838.0 eV was attributed to the final state of La 3d<sub>5/2</sub> on La<sub>2</sub>O<sub>3</sub> [29], indicating that La was present in the form of La<sup>3+</sup> on the sample surface. The signal at BE = 176.1 eV was attributed to the Tm<sup>3+</sup> species on the surface of Tm/NaSep [30]. Therefore, all of the rare earth ions in the oxides were present in the form of RE<sup>3+</sup>.

Two peaks in O 1s XPS spectrum of each of the NaSep and RE/NaSep samples appeared at BE = 531.2 and 532.4 eV, representing the surface lattice oxygen (O<sub>latt</sub>) and adsorbed oxygen (O<sub>ads</sub>, for example, O<sub>2</sub><sup>-</sup>, O<sub>2</sub><sup>2-</sup>, O<sup>-</sup> and/or OH) species [31]. The O<sub>ads</sub>/O<sub>latt</sub> atomic ratios are summarized in Table 2. After loading of rare earth oxides, the O<sub>ads</sub>/O<sub>latt</sub> atomic ratio increased significantly. The O<sub>ads</sub>/O<sub>latt</sub> atomic ratio decreased in the order of Eu/NaSep (7.33) > Dy/NaSep (5.66) > La/NaSep (4.53) > Tm/NaSep (3.93) > NaSep (2.33). According to the literature [32,33], the O<sub>ads</sub> species were closely related to the catalytic activity of a sample. The higher the O<sub>ads</sub> concentration, the better was the catalytic activity. Obviously, the Eu/NaSep sample is expected to show the best performance for HCHO oxidation, as confirmed in the activity evaluation.



**Figure 4.** SEM images of (a) Eu/NaSep, (b) Dy/NaSep, (c) La/NaSep, (d) Tm/NaSep and (e) NaSep.

**Table 2.** Reduction temperatures, H<sub>2</sub> consumption, and O<sub>ads</sub>/O<sub>latt</sub> atomic ratios of the samples.

Sample	Temperature (°C)		H <sub>2</sub> Consumption (mmol/g <sub>cat</sub> )			O <sub>ads</sub> /O <sub>latt</sub> Atomic Ratio
	Peak 1	Peak 2	Peak 1	Peak 2	Total	
NaSep	–	633	–	0.128	0.128	2.33
La/NaSep	458	621	0.148	0.459	0.607	4.53
Eu/NaSep	456	620	0.179	0.529	0.708	7.33
Dy/NaSep	456	619	0.169	0.476	0.645	5.66
Tm/NaSep	474	626	0.166	0.33	0.496	3.93

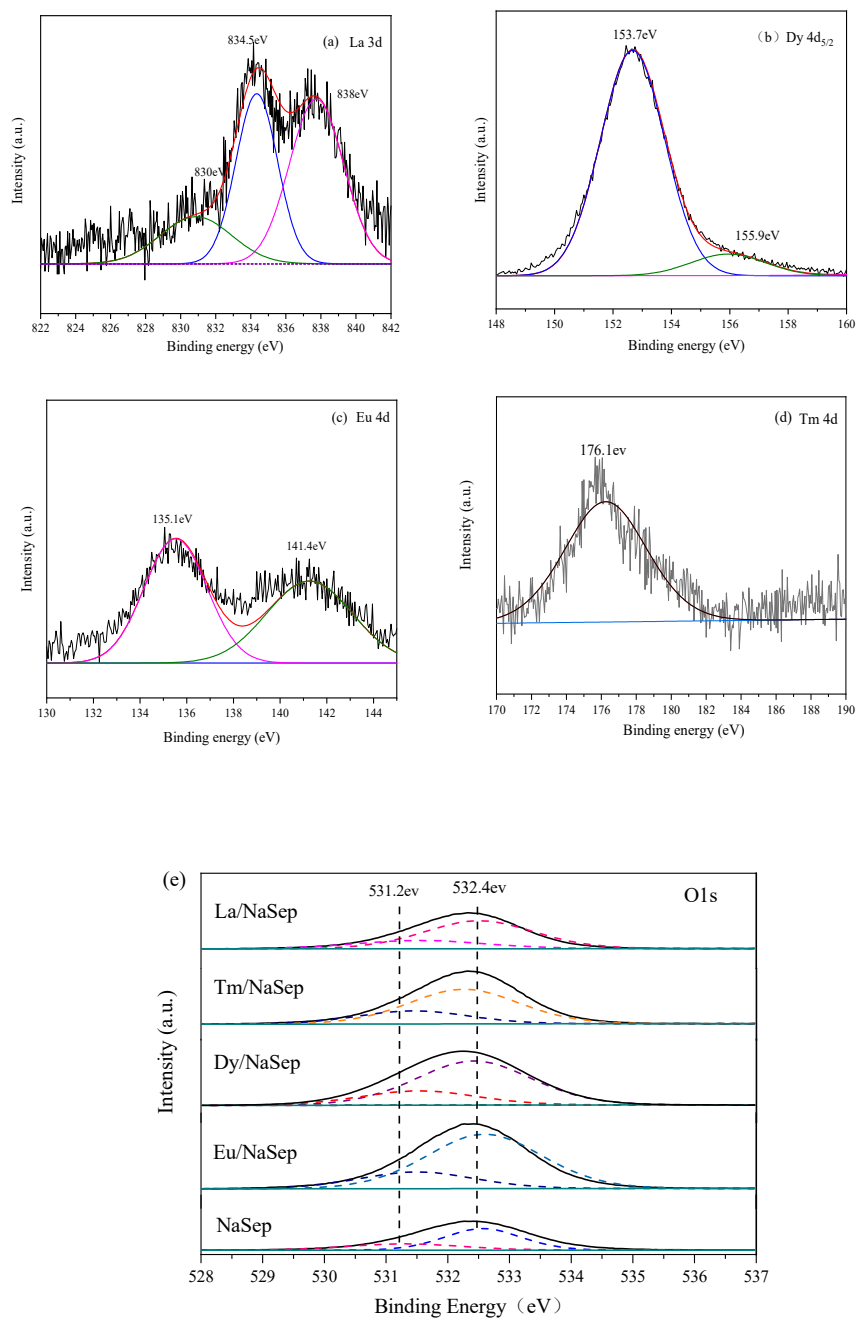


**Figure 5.** (a) La 3d, (b) Dy 4d<sub>5/2</sub>, (c) Eu 4d, (d) Tm 3d, and (e) O 1s XPS spectra of the samples.

#### 2.4. Reducibility

H<sub>2</sub>-TPR was used to evaluate the reducibility of the samples, and their profiles are illustrated in Figure 6. For the NaSep sample, a reduction peak was observed at 633 °C. According to the XRF analysis results, we can see that in addition to SiO<sub>2</sub>, Al<sub>2</sub>O<sub>3</sub>, and MgO in sepiolite which were difficult to be reduced, the iron oxide (2.33 wt %) could be reduced from Fe<sub>2</sub>O<sub>3</sub> to Fe<sup>0</sup> in NaSep [34].

The reduction peaks of RE/NaSep appeared at 454–474 and 619–626 °C, respectively. The low-temperature peak at 454–474 °C was attributed to the removal of the surface adsorbed oxygen species, while the high-temperature peak at 619–626 °C was due to reduction of the iron oxide species. The RE/NaSep samples displayed a lower reduction temperature than the NaSep support (633 °C), which might be due to the synergistic effect of the rare earth oxide and iron oxide [35].

Peak temperatures and H<sub>2</sub> consumption of the samples are listed in Table 2. After loading of the rare earth oxides, the total hydrogen consumption significantly increased and followed an order of Eu/NaSep (0.708 mmol/g) > Dy/NaSep (0.645 mmol/g) > La/NaSep (0.607 mmol/g) > Tm/NaSep (0.496 mmol/g) > NaSep (0.128 mmol/g). Combining the previous results, we can realize that after loading of the rare earth oxide, the reduction peak was shifted to a lower temperature and the peak area increased. The Eu/NaSep sample showed the lowest reduction temperature and the largest hydrogen consumption, indicating that this sample possessed the best reducibility, which was consistent with the catalytic activity sequence of HCHO oxidation.

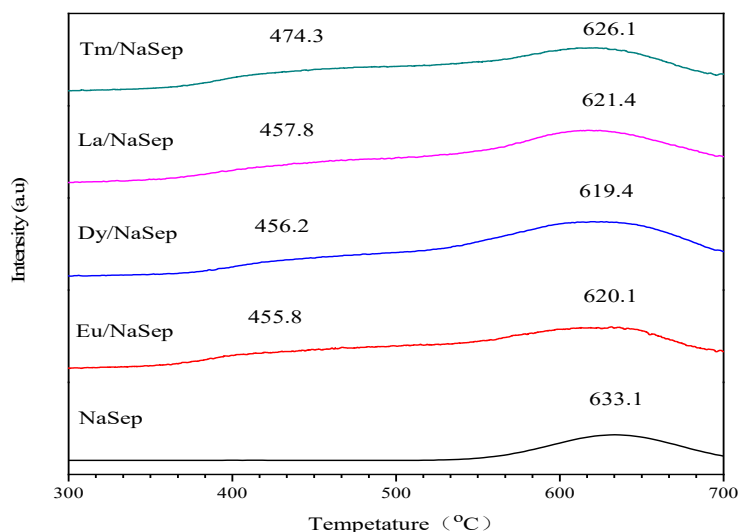


Figure 6. H<sub>2</sub>-TPR profiles of the samples.

### 2.5. Surface Acid Property

Sepiolite is rich in the hydroxyl group, which can produce a more amount of the Brønsted acid sites. According to the literature [36], adsorption of NH<sub>3</sub> at the Brønsted acid sites (–OH) to form the –NH<sub>4</sub><sup>+</sup> species, and the result of NH<sub>3</sub>-TPD characterization proved the presence of hydroxyl groups in the sample. A larger amount of hydroxyl groups could offer more opportunity for HCHO adsorption on the sample surface and improve the catalytic activity of HCHO oxidation.

NH<sub>3</sub>-TPD is frequently used to determine the surface acidity of a catalyst. Figure 7 shows NH<sub>3</sub>-TPD profiles of the NaSep and RE/NaSep samples. Each profile could be decomposed into three desorption stages of 150–220, 220–300, and 300–450 °C, corresponding to the weak, medium, and strong acid sites. The weak peak at 150–220 °C was due to desorption of the physically adsorbed NH<sub>3</sub> and some NH<sub>4</sub><sup>+</sup> bound to the weak Brønsted acid sites, the medium one at 220–300 °C was attributed to desorption of the NH<sub>4</sub><sup>+</sup> bound to the strong Brønsted acid sites [37], and the last strong peak above 300 °C was assigned to desorption of the NH<sub>3</sub> coordinated with the Lewis acid sites [38].

After the rare earth oxide was loaded, the NH<sub>3</sub> adsorption amount obviously increased, especially on the samples with weak and medium acid sites, indicating that the rare earth oxide provided a more amount of the Brønsted acid sites. The amount of the Lewis acid sites above 300 °C also increased, which was also due to loading of the rare earth oxide. Therefore, loading of the rare earth oxide led to a significant increase in amounts of the medium and strong acid sites, thus increasing the total amount of the acid sites. As shown in Table 3, the order of total acidity was Eu/NaSep (53 μmol/g) > Dy/NaSep (42 μmol/g) > La/NaSep (32 μmol/g) > Tm/NaSep (28 μmol/g) > NaSep (24 μmol/g). As compared with the other samples, Eu/NaSep possessed the highest total acidity. The sequence in acid amount also coincided with the catalytic activity order of these samples for HCHO oxidation.

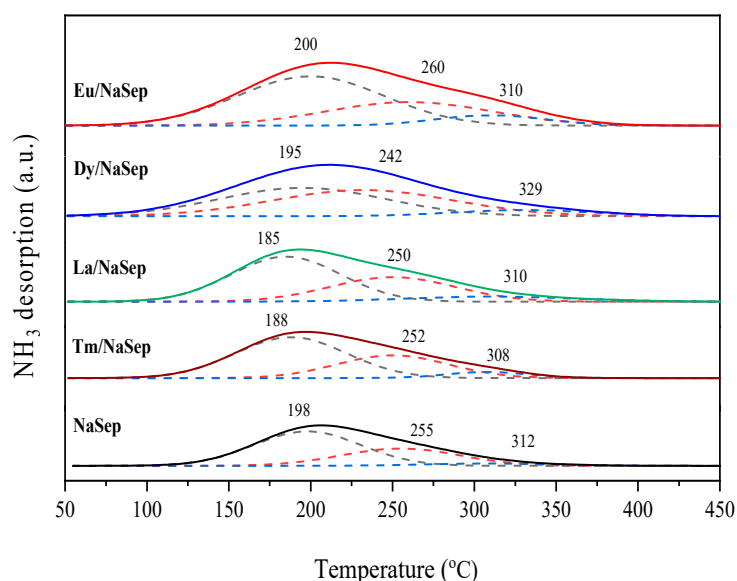


**Figure 7.** NH<sub>3</sub>-TPD profiles of the samples.

**Table 3.** Ammonia uptakes of the samples.

Sample	Ammonia Uptake (μmol/g)			
	Weak (150–220 °C)	Medium (220–300 °C)	Strong (300–450 °C)	Total
NaSep	14	9	1	24
La/NaSep	17	12	3	32
Eu/NaSep	25	22	6	53
Dy/NaSep	19	19	4	42
Tm/NaSep	15	11	2	28

## 2.6. Catalytic Performance

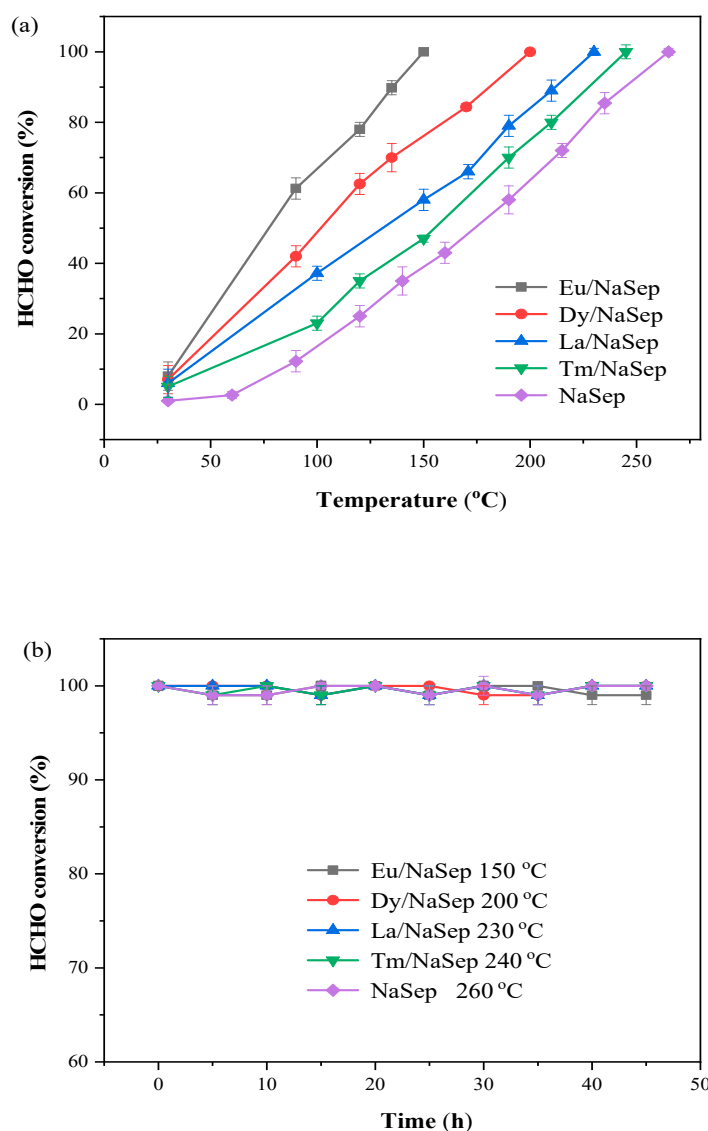
Catalytic activities over  $x$ Eu/NaSep ( $x = 1.0, 3.0, 5.0,$  and  $7.0$  wt %) for HCHO oxidation are shown in Figure S1. Among all of the  $x$ Eu/NaSep catalysts, the one at a 5.0 wt % Eu loading exhibited the best activity. Therefore, an Eu loading of 5.0 wt % was selected for further study.

Figure 8a shows catalytic activities of the NaSep and TM/NaSep samples for the oxidation of HCHO. The reaction temperatures ( $T_{100\%}$ ) required to achieve an HCHO conversion of 100% were applied to evaluate the catalytic activities of the samples. The blank test (in which only quartz sand was loaded in the microreactor) showed that no significant HCHO conversions were detected below 250 °C. In other words, HCHO and O<sub>2</sub> did not remarkably react below 250 °C in the absence of a catalyst.

It can be seen from Figure 8a that the complete conversion of HCHO over the NaSep sample was achieved at 260 °C. After loading of the rare earth oxide, catalytic activity was obviously improved, and its sequence was Eu/NaSep > Dy/NaSep > La/NaSep > Tm/NaSep > NaSep. Among all of the samples, Eu/NaSep exhibited the highest catalytic activity, with a  $T_{100\%}$  of 150 °C for HCHO oxidation.

According to the previous study [39], we used the reaction rate ( $r_{\text{cat}}$ ) to compare the inherent catalytic activities of the samples. The  $r_{\text{cat}}$  (mol/(g<sub>cat</sub> s)) is defined as the molar amount of HCHO converted per gram of catalyst per second. The  $r_{\text{cat}}$  values of HCHO oxidation at 100 °C over the samples are summarized in Table 4. The  $r_{\text{cat}}$  values ( $3.54 \times 10^{-6}$ – $1.47 \times 10^{-6}$  mol/(g<sub>cat</sub> s)) for HCHO oxidation at 100 °C over RE/NaSep were much higher than those of the other rare earth oxide-based catalysts, such as ( $9.20 \times 10^{-8}$  mol/(g<sub>cat</sub> s)) over 24Mn-19Co-1Ce at 100 °C, ( $5.11 \times 10^{-7}$  mol/(g<sub>cat</sub> s)) over 2.5Au/CeO<sub>2</sub> at 100 °C [40], and ( $4.77 \times 10^{-8}$  mol/(g<sub>cat</sub> s)) over Mn-Cu-Ce at 100 °C [41]. Compared with the other supported transition metal catalysts, the  $r_{\text{cat}}$  values ( $1.47 \times 10^{-6}$ – $3.54 \times 10^{-6}$  mol/(g<sub>cat</sub> s)) of the RE/NaSep samples were much higher than that ( $2.55 \times 10^{-8}$  mol/(g<sub>cat</sub> s)) of Cu-Mn/TiO<sub>2</sub> and that ( $3.06 \times 10^{-8}$  mol/(g<sub>cat</sub> s)) of Cu-Mn/ $\gamma$ -Al<sub>2</sub>O<sub>3</sub> [42]. Moreover, the  $r_{\text{cat}}$  value decreased in the order of

Eu/NaSep > Dy/NaSep > La/NaSep > Tm/NaSep > NaSep, which was in good consistency with the changing trend in the catalytic activity of the samples.



**Figure 8.** (a) HCHO conversion as a function of temperature and (b) HCHO conversion versus reaction time over the samples under the conditions of 2000 ppm HCHO + 20 vol % O<sub>2</sub> + N<sub>2</sub> (balance) and GHSV = 240,000 mL/(g h).

**Table 4.** A comparison on specific reaction rates ( $r_{\text{cat}}$ ) of formaldehyde (HCHO) oxidation at 100 °C over the catalysts studied in the present work and reported in the literature.

Catalyst	$r_{\text{cat}}$ (mol/(g <sub>cat</sub> s))	Ref.
Eu/NaSep	$3.54 \times 10^{-6}$	This study
Dy/NaSep	$2.29 \times 10^{-6}$	This study
La/NaSep	$1.74 \times 10^{-6}$	This study
Tm/NaSep	$1.47 \times 10^{-6}$	This study
NaSep	$4.36 \times 10^{-7}$	This study
24Mn-19Co-1Ce	$9.20 \times 10^{-8}$	[40]
2.5Au/CeO <sub>2</sub>	$5.11 \times 10^{-7}$	[40]
Mn-Cu-Ce mixed oxide	$4.77 \times 10^{-8}$	[41]
Cu-Mn/TiO <sub>2</sub>	$2.55 \times 10^{-8}$	[42]
Cu-Mn/ $\gamma$ -Al <sub>2</sub> O <sub>3</sub>	$3.06 \times 10^{-8}$	[42]

Figure 8b shows the catalytic stability of all of the samples after 45 h of HCHO oxidation. It can be seen that catalytic activities over all of the samples were not altered significantly within 45 h of reaction, indicating that these materials possessed good catalytic stability under the adopted reaction conditions.

### 2.7. In Situ DRIFTS and Catalytic Oxidation Mechanism

In order to study the reaction mechanism, the in situ DRIFTS technique was employed to investigate HCHO oxidation over the Eu/NaSep sample. Figure 9a shows the in situ DRIFT spectra of the Eu/NaSep sample exposed to 2000 ppm HCHO + N<sub>2</sub> without O<sub>2</sub> at 30 °C for 1 h. The absorption bands at 3507, 2983, 1713, 1633, 1590, 1453, and 1390 cm<sup>-1</sup> were observed. As the adsorption time increased, the band strength began to increase and reached a stable level after 1 h. According to the literature [43], the band at 3507 cm<sup>-1</sup> was assigned to the stretching vibration of the hydroxyl group, the ones at 2983, 1590, and 1390 cm<sup>-1</sup> were attributed to the formate species on the surface of the sample, the band at 2983 cm<sup>-1</sup> was ascribed to the stretching vibration of C–H bond, and the ones at 1590 and 1390 cm<sup>-1</sup> were due to the  $\nu_{as}(\text{COO}^-)$  and  $\delta(\text{CH})$ , respectively [44]. The band at 1633 cm<sup>-1</sup> was due to adsorbed water on the catalyst surface, and the band at 1713 cm<sup>-1</sup> was ascribed to the  $\nu(\text{C=O})$  of carbonate species [45]. Moreover, the band at 1453 cm<sup>-1</sup> was due to the dioxymethylene (DOM) [46]. Therefore, the adsorbed HCHO on the sample surface could form the formate species in the absence of O<sub>2</sub>, which might be due to the fact that the sample surface contained a large amount of the adsorbed oxygen species, which was consistent with the above results.

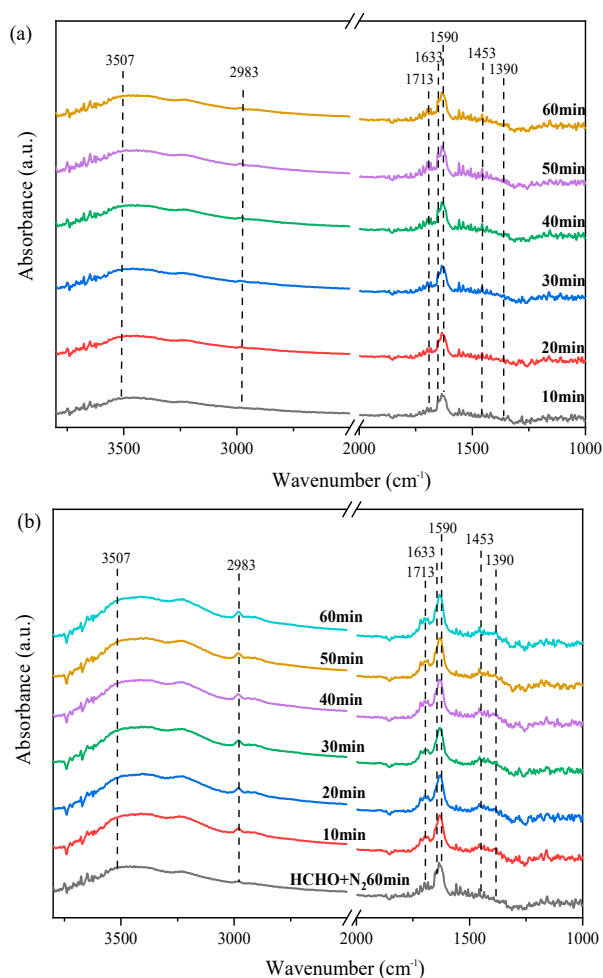


**Figure 9.** (a) In situ DRIFTS spectra of HCHO adsorption on the Eu/NaSep sample under the condition of 30 °C and 2000 ppm HCHO + N<sub>2</sub> (balance), and (b) in situ DRIFTS spectra of the Eu/NaSep sample in a flow of 2000 ppm HCHO + 20 vol % O<sub>2</sub> + N<sub>2</sub> (balance) at 30 °C and different time.

Figure 9b shows the intermediate species on the surface of the sample after exposure to 2000 ppm HCHO + N<sub>2</sub> + O<sub>2</sub> at 30 °C. Almost all of the characteristic bands increased in intensity, as compared with the above HCHO adsorption without O<sub>2</sub> on the sample surface. Among them, the intensity of the bands (2983 and 1590 cm<sup>-1</sup>) assignable to the formate species increased significantly, as compared with that of the other characteristic bands. This was because, in the presence of oxygen, HCHO could be more adsorbed on the sample surface and form the formate species. However, the DOM species were hardly changed (i.e., no DOM species (1453 cm<sup>-1</sup>) formation), which indicates that the Eu/NaSep sample was capable of rapidly converting the HCHO adsorbed on the sample surface. According to the literature [47], when HCHO was oxidized, it was first converted to the DOM species, and then the formate species was generated immediately. Moreover, with the oxidation of HCHO, the intensity of the band (3507 cm<sup>-1</sup>) of the hydroxyl group increased significantly. Therefore, HCHO could be rapidly oxidized to the formate species on the surface of the sample, demonstrating that the adsorbed HCHO was converted to the formate species according to Equations (1) and (2) [46]:

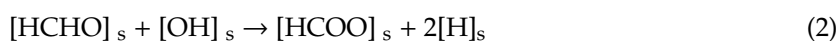
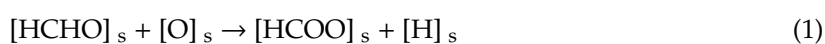


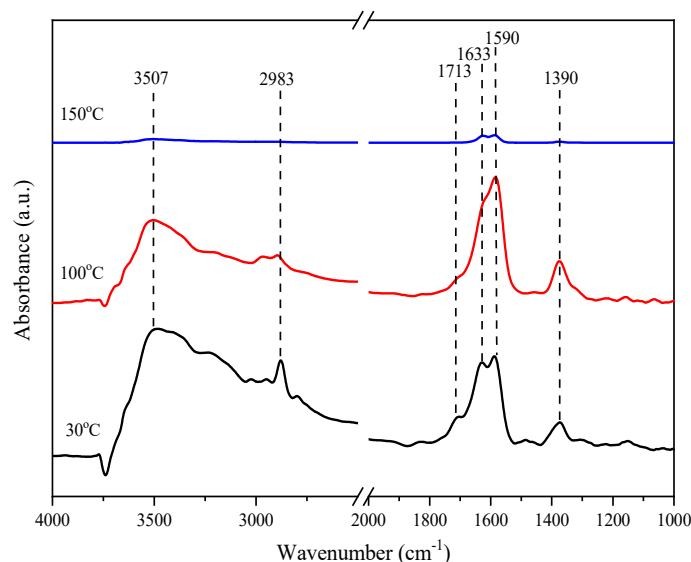
Figure S2 shows the in situ DRIFTS spectra of the Eu/NaSep and NaSep samples for the oxidation of HCHO at 30 °C. It can be realized that the intermediate products formed over the NaSep sample (Figure S2b) were the same as those formed over the Eu/NaSep sample (Figure S2a), but absorption band intensity (i.e., the corresponding amounts) of the intermediate products over the former was lower than that over the latter.

Figure 10 shows the oxidation of the intermediates formed via HCHO oxidation over the Eu/NaSep sample at different temperatures. Catalytic oxidation of HCHO at 30 °C is shown in Figure 10b. The HCHO was rapidly decomposed into the formate (1590 and 1390 cm<sup>-1</sup>) and carbonate (1713 cm<sup>-1</sup>) species on the Eu/NaSep surface. When the temperature rose to 100 °C, a significant decrease in band intensity of the formate species (1590 and 1390 cm<sup>-1</sup>) was observed, indicating a rapid increase in the decomposition rate of the formate species. The characteristic band (3507 cm<sup>-1</sup>) intensity of the hydroxyl group also began to drop, indicating that the hydroxyl group played an important role in the oxidation of HCHO. Generally, abundant hydroxyl groups can provide a more amount of the sites for HCHO adsorption and promote the oxidation of formate species. The characteristic band intensity of the carbonate species increased at the same time, indicating that the formate species were decomposed on the surface of the sample to form the carbonate species. When the temperature reached 150 °C, the intermediate products (e.g., the formate (1590 and 1390 cm<sup>-1</sup>) and carbonate (1713 cm<sup>-1</sup>) species) disappeared almost completely, indicating that HCHO was totally oxidized at this temperature, which was in good agreement with the reaction temperature in HCHO oxidation of the Eu/NaSep sample.

As a result, compared with NaSep, loading of the rare earth oxide significantly improved the catalytic activity of HCHO oxidation. It was confirmed by the FTIR results that sepiolite was rich in the hydroxyl group. From the in situ DRIFTS results, it was found that hydroxyl groups could quickly adsorb HCHO on the sample surface, and loading of the rare earth oxide could generate a more amount of oxygen vacancies that served as the active sites for HCHO oxidation, as evidenced by its highest O<sub>ads</sub>/O<sub>latt</sub> atomic ratio revealed by the XPS analysis. The above results show that Eu/NaSep exhibited the best catalytic activity, which was due to the large number of hydroxyl species (Figure 3), the lowest reduction temperature (ca. 456 °C), the highest O<sub>ads</sub>/O<sub>latt</sub> atomic ratio (7.33), and the highest acidity (53 μmol/g).

A possible mechanism for HCHO oxidation over Eu/NaSep is presented in Figure 11. Firstly, HCHO was adsorbed on the surface of the sample, then the surface adsorbed HCHO was oxidized to the DOM intermediate by the adsorbed oxygen species, and finally oxidized to the formate species rapidly. The hydroxyl groups in sepiolite could not only promote the adsorption of HCHO on the

sample surface, but also accelerate the formation and decomposition of the formate species. Finally, the carbonate species derived from the oxidation of the formate species were eventually converted to  $\text{CO}_2$  and  $\text{H}_2\text{O}$ . Therefore, the total oxidation of HCHO over the sample surface was as follows:



**Figure 10.** In situ DRIFTS spectra of the Eu/NaSep sample after 1 h of HCHO oxidation at 30, 100, and 150 °C.

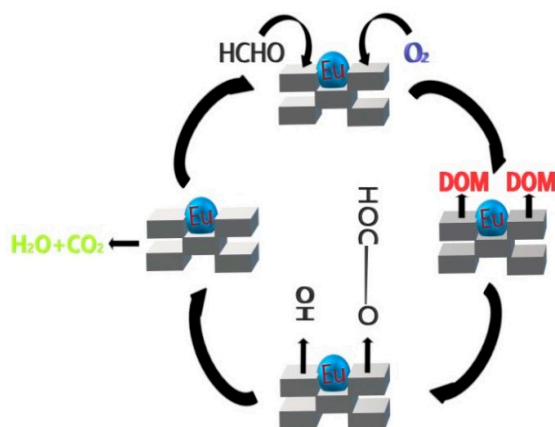


**Figure 11.** Proposed mechanism of HCHO oxidation over the Eu/NaSep sample.

### 3. Experimental

#### 3.1. Catalyst Preparation

The sepiolite raw material was bought from Liuyang Sepiolite Mining Industry Company (China). The support was obtained via leaching of the sepiolite with sodium. Sodium modification of sepiolite is expected to improve the thermal stability of the sample, the cation exchange capacity was significantly enhanced, and the original structure of sepiolite was not changed. The chemical composition of sepiolite and the sodium-treated procedures are described in the Supplementary material. It is well known that different raw sepiolites may differ slightly in composition. However, after the sepiolite was modified with sodium, its physical property was determined. Therefore, the present study used

the sodium-modified sepiolite to load the rare earth elements, and explored the effect of different rare earth elements on the catalytic activity of the sodium-modified sepiolite for HCHO oxidation.

The  $x\text{Eu}/\text{NaSep}$  ( $x = 1.0, 3.0, 5.0,$  and  $7.0$  wt %) catalysts were prepared using the rotary evaporation method. The wet samples were dried for 24 h and calcined at  $400\text{ }^\circ\text{C}$  for 2 h, and the obtained samples were denoted as  $x\text{Eu}/\text{NaSep}$ , and their catalytic activities for HCHO oxidation are shown in Figure S1.

The NaSep-supported rare earth oxides (theoretical rare earth oxide loading = 5.0 wt %) were prepared using the rotary evaporation method with nitrates of La, Eu, Dy, and Tm (A.R., Beijing Chemical Co., Ltd.) as metal precursors, respectively. The samples were at  $80\text{ }^\circ\text{C}$  dried for 24 h and calcined at  $400\text{ }^\circ\text{C}$  for 2 h. The obtained samples were denoted as RE/NaSep (RE = La, Eu, Dy, and Tm). The synthetic yield of all catalyst samples was 92% to 94%.

### 3.2. Catalyst Characterization

X-ray diffraction (XRD) patterns of the samples were measured on a Bruker D8-Advance apparatus in the  $2\theta$  range of  $5\text{--}80^\circ$  ( $\lambda = 0.15404$  nm at a scan rate of  $5^\circ/\text{min}$ ). Nitrogen sorption isotherms were obtained at liquid nitrogen temperature ( $-196\text{ }^\circ\text{C}$ ) on a JW-BK200C apparatus (Beijing, China). Specific surface areas of the samples were calculated using the Brunauer–Emmett–Teller (BET) equation, and their pore-size distributions were determined using the desorption branch data of the isotherms by the Barrett–Joyner–Halenda (BJH) method.

Hydrogen temperature-programmed reduction ( $\text{H}_2\text{-TPR}$ ) of the samples was conducted on a Builder PCA-1200 analyzer. Before the  $\text{H}_2\text{-TPR}$  experiment, the sample (100 mg) was first treated in a flow (30 mL/min) of the 5 vol %  $\text{O}_2/\text{N}_2$  mixture at  $400\text{ }^\circ\text{C}$  for 1 h, and then cooled to room temperature (RT). The sample was finally reduced in a flow (30 mL/min) of the 5 vol %  $\text{H}_2/\text{N}_2$  mixture at a heating rate of  $10\text{ }^\circ\text{C}/\text{min}$  from RT to  $1000\text{ }^\circ\text{C}$ . The reduction peaks were calibrated against that of the reduction of a powdered CuO sample (Aldrich, 99.995%).

X-ray photoelectron spectroscopic (XPS) spectra of the samples were recorded on a Thermo ESCALAB 250Xi electron spectrometer (Shanghai, China) equipped with an Al  $K\alpha$  X-ray source and a hemispherical electron analyzer operating at constant pass energy (30.0 eV).

Fourier transform infrared (FTIR) spectra of the samples were obtained on an FTIR spectrometer (Thermo Scientific Nicolet 6700, Waltham, America). The in situ diffuse reflectance infrared spectroscopic (DRIFTS) experiments were conducted on a Bruker Tensor II spectrometer (Karlsruhe, Germany), in which there was a high-temperature reaction chamber (Harrick Praying Mantis). The sample packed in a cup of the reaction chamber was heated to  $400\text{ }^\circ\text{C}$  at a total  $\text{N}_2$  flow of 200 mL/min for 1 h to remove the adsorbed impurities. Each of the spectra had a resolution of  $4\text{ cm}^{-1}$  and accumulated 32 scans.

### 3.3. Catalytic Activity Evaluation

HCHO oxidation activity was evaluated by loading the sample (50 mg) well mixed with quartz sand (150 mg) in a fixed-bed quartz tubular microreactor. The reactant mixture was 2000 ppm HCHO + 20 vol %  $\text{O}_2 + \text{N}_2$  (balance) and the GHSV was 240,000 mL/(g h). The HCHO concentration was analyzed online on a Techcomp GC-7900 gas chromatograph (Shanghai, China) equipped with a flame ion detector (FID). The conversion of HCHO ( $X_{\text{HCHO}}$ ) was calculated according to the changes in HCHO concentration ( $C_{\text{HCHO,inlet}}$  and  $C_{\text{HCHO,outlet}}$ ) of the inlet and outlet gas mixture, as shown below:

$$X_{\text{HCHO}} = \frac{C_{\text{HCHO,inlet}} - C_{\text{HCHO,outlet}}}{C_{\text{HCHO,inlet}}} \times 100\%$$

The detailed measurement procedures are stated in the Supplementary Materials.

#### 4. Conclusions

After loading the rare earth oxide, the redox properties of the NaSep sample changed greatly, especially for the Eu/NaSep sample. According to the characterization results, we can know that loading of  $\text{Eu}_2\text{O}_3$  greatly increased the amount of the surface oxygen vacancies, which enabled gas-phase oxygen molecules to form the adsorbed oxygen species on the sample surface and promoted the oxidation of HCHO. This work provided evidence that the Eu/NaSep sample possessed the highest atomic ratio of  $O_{\text{ads}}/O_{\text{latt}}$  among all of the samples. As revealed by the  $\text{H}_2$ -TPR characterization results, the Eu/NaSep sample exhibited the best reducibility, which contributed to the good catalytic activity for HCHO oxidation of the sample. HCHO oxidation took place via the steps of  $\text{HCHO} + \text{O}_2 \rightarrow \text{HCOO}^- + \text{OH}^- \rightarrow \text{H}_2\text{O} + \text{CO}_2$ . Therefore, the highest  $O_{\text{ads}}/O_{\text{latt}}$  atomic ratio, the largest amount of hydroxyl groups, the highest acidity, and the best reducibility was accountable for the optimal catalytic activity of Eu/NaSep.

**Supplementary Materials:** The following are available online at <http://www.mdpi.com/2073-4344/10/3/328/s1>, Figure S1. HCHO conversion as a function of temperature over the x wt % Eu/NaSep sample under the conditions of 2000 ppm HCHO + 20 vol %  $\text{O}_2 + \text{N}_2$  (balance) and GHSV = 240,000 mL/(g h). Figure S2. In situ DRIFTS spectra of (a) Eu/NaSep, and (b) NaSep exposed to the flow of 2000 ppm HCHO + 20 vol %  $\text{O}_2 + \text{N}_2$  (balance) at 30 °C and different time.

**Author Contributions:** Conceptualization, Q.Y.; methodology, N.D. and M.C.; software, N.D. and M.C.; investigation, N.D. and M.C.; resources, Q.Y.; data curation, N.D. and M.C.; writing—original draft preparation, N.D.; writing—review and editing, Q.Y. and H.D.; visualization, S.C. and T.K.; supervision, Q.Y. and H.D.; project administration, Q.Y.; funding acquisition, Q.Y. All authors have read and agreed to the published version of the manuscript.

**Funding:** This work was supported by the National Natural Science Foundation of China (21277008 and 20777005), the National Key Research and Development Program of China (2017YFC0209905), and the Natural Science Foundation of Beijing (8082008). We also thank Prof. Ralph T. Yang (University of Michigan) for his helpful discussion and encouragement.

**Conflicts of Interest:** The authors declare no conflicts of interest.

#### References

- Lin, M.; Yu, X.; Yang, X.; Ma, X.; Ge, M. Exploration of the active phase of the hydrotalcite-derived cobalt catalyst for HCHO oxidation. *Chin. J. Catal.* **2019**, *40*, 703–712. [[CrossRef](#)]
- Weng, X.; Long, Y.; Wang, W.; Shao, M.; Wu, Z. Structural effect and reaction mechanism of  $\text{MnO}_2$  catalysts in the catalytic oxidation of chlorinated aromatics. *Chin. J. Catal.* **2019**, *40*, 638–646. [[CrossRef](#)]
- Bai, B.; Qiao, Q.; Li, Y.; Peng, Y.; Li, J. Effect of pore size in mesoporous  $\text{MnO}_2$  prepared by KIT-6 aged at different temperatures on ethanol catalytic oxidation. *Chin. J. Catal.* **2018**, *39*, 630–638. [[CrossRef](#)]
- Liu, Y.; Deng, J.; Xie, S.; Wang, Z.; Dai, H. Catalytic removal of volatile organic compounds using ordered porous transition metal oxide and supported noble metal catalysts. *Chin. J. Catal.* **2016**, *37*, 1193–1205. [[CrossRef](#)]
- Zhang, M.; Li, C.; Qu, L.; Fu, M.; Zeng, G.; Fan, C.; Ma, J.; Zhan, F. Catalytic oxidation of NO with  $\text{O}_2$  over  $\text{FeMnO}_x/\text{TiO}_2$ : Effect of iron and manganese oxides loading sequences and the catalytic mechanism study. *Appl. Surf. Sci.* **2014**, *300*, 58–65. [[CrossRef](#)]
- Zhu, X.; Gao, X.; Qin, R.; Zeng, Y.; Qu, R.; Zheng, C.; Tu, X. Plasma-catalytic removal of formaldehyde over Cu–Ce catalysts in a dielectric barrier discharge reactor. *Appl. Catal. B* **2015**, *170*, 293–300. [[CrossRef](#)]
- Sun, Y.; Qu, Z.; Chen, D.; Wang, H.; Zhang, F.; Fu, Q. Formaldehyde catalytic oxidation over hydroxyapatite modified with various organic molecules. *Chin. J. Catal.* **2014**, *35*, 1927–1936. [[CrossRef](#)]
- Bai, B.; Qiao, Q.; Li, J.; Hao, J. Progress in research on catalysts for catalytic oxidation of formaldehyde. *Chin. J. Catal.* **2016**, *37*, 102–122. [[CrossRef](#)]
- Imamura, S.; Uchihori, D.; Utani, K.; Ito, T. Oxidative decomposition of formaldehyde on silver-cerium composite oxide catalyst. *Catal. Lett.* **1994**, *24*, 377–384. [[CrossRef](#)]
- Álvarez-Galván, M.C.; De la Peña O’Shea, V.A.; Fierro, J.L.G.; Arias, P.L. Alumina-supported manganese- and manganese–palladium oxide catalysts for VOCs combustion. *Catal. Commun.* **2003**, *4*, 223–228. [[CrossRef](#)]

11. Guo, H.; Zhang, H.; Peng, F.; Yang, H.; Xiong, L.; Wang, C.; Huang, C.; Chen, X.; Ma, L. Effects of Cu/Fe ratio on structure and performance of attapulgite supported CuFeCo-based catalyst for mixed alcohols synthesis from syngas. *Appl. Catal. A* **2015**, *503*, 51–61. [[CrossRef](#)]
12. Bu, Y.; Chen, Y.; Jiang, G.; Hou, X.; Li, S.; Zhang, Z. Understanding of Au-CeO<sub>2</sub> interface and its role in catalytic oxidation of formaldehyde. *Appl. Catal. B* **2020**, *260*, 118–138. [[CrossRef](#)]
13. Yu, S.; Liu, X.; Xu, G.; Qiu, Y.; Cheng, L. Magnetic Fe<sub>3</sub>O<sub>4</sub>/sepiolite composite synthesized by chemical co-precipitation method for efficient removal of Eu(III). *Desalin. Water Treat.* **2016**, *57*, 16943–16954. [[CrossRef](#)]
14. Song, Y.; Liu, L.; Fu, Z.; Ye, Q.; Cheng, S.; Kang, T.; Dai, H. Excellent performance of Cu-Mn/Ti-sepiolite catalysts for low-temperature CO oxidation. *Front. Environ. Sci. Eng.* **2017**, *11*, 5. [[CrossRef](#)]
15. Ma, Y.; Zhang, G. Sepiolite nanofiber-supported platinum nanoparticle catalysts toward the catalytic oxidation of formaldehyde at ambient temperature: Efficient and stable performance and mechanism. *Chem. Eng. J.* **2016**, *288*, 70–78. [[CrossRef](#)]
16. Zhang, G.; Xiong, Q.; Xu, W.; Guo, S. Synthesis of bicrystalline TiO<sub>2</sub> supported sepiolite fibers and their photocatalytic activity for degradation of gaseous formaldehyde. *Appl. Clay Sci.* **2014**, *102*, 231–237. [[CrossRef](#)]
17. Ye, Q.; Yan, L.; Wang, H.; Cheng, S.; Wang, D.; Kang, T.; Dai, H. Enhanced catalytic performance of rare earth-doped Cu/H-Sep for the selective catalytic reduction of NO with C<sub>3</sub>H<sub>6</sub>. *Appl. Catal. A* **2012**, *431*, 42–48. [[CrossRef](#)]
18. Rytwo, G.; Tropp, D.; Serban, C. Adsorption of diquat, paraquat and methyl green on sepiolite: Experimental results and model calculations. *Appl. Clay Sci.* **2002**, *20*, 273–282. [[CrossRef](#)]
19. Sabah, E.; Çelik, M.S. Interaction of Pyridine Derivatives with Sepiolite. *J. Colloid Interf. Sci.* **2002**, *251*, 33–38. [[CrossRef](#)]
20. Alkan, M.; Tekin, G.; Namli, H. FTIR and zeta potential measurements of sepiolite treated with some organosilanes. *Micropor. Mesopor. Mat.* **2005**, *84*, 75–83. [[CrossRef](#)]
21. Casal, B.; Merino, J.; Serratos, J.; Ruiz-Hitzky, E. Sepiolite-based materials for the photo-and thermal-stabilization of pesticides. *Appl. Clay Sci.* **2001**, *18*, 245–254. [[CrossRef](#)]
22. Gao, Y.; Gan, H.; Zhang, G.; Guo, Y. Visible light assisted Fenton-like degradation of rhodamine B and 4-nitrophenol solutions with a stable poly-hydroxyl-iron/sepiolite catalyst. *Chem. Eng. J.* **2013**, *217*, 221–230. [[CrossRef](#)]
23. Özcan, A.; Özcan, A.S. Adsorption of Acid Red 57 from aqueous solutions onto surfactant-modified sepiolite. *J. Hazard. Mater.* **2005**, *125*, 252–259. [[CrossRef](#)] [[PubMed](#)]
24. Yuan, P.; Yin, X.; He, H.; Yang, D.; Wang, L.; Zhu, J. Investigation on the delaminated-pillared structure of TiO<sub>2</sub>-PILC synthesized by TiCl<sub>4</sub> hydrolysis method. *Micropor. Mesopor. Mat.* **2006**, *93*, 240–247. [[CrossRef](#)]
25. Qiao, N.; Zhang, X.; He, C.; Li, Y.; Zhang, Z.; Cheng, J.; Hao, Z. Enhanced performances in catalytic oxidation of o-xylene over hierarchical macro-/mesoporous silica-supported palladium catalysts. *Front. Environ. Sci. Eng.* **2016**, *10*, 458–466. [[CrossRef](#)]
26. Belessi, V.; Lambropoulou, D.; Konstantinou, I.; Katsoulidis, A.; Pomonis, P.; Petridis, D.; Albanis, T. Structure and photocatalytic performance of TiO<sub>2</sub>/clay nanocomposites for the degradation of dimethachlor. *Appl. Catal. B* **2007**, *73*, 292–299. [[CrossRef](#)]
27. Barreca, D.; Gasparotto, A.; Milanov, A.; Tondello, E.; Devi, A.; Fischer, R.A. Nanostructured Dy<sub>2</sub>O<sub>3</sub> films: An XPS Investigation. *Surf. Sci. Spectra.* **2007**, *14*, 52–59. [[CrossRef](#)]
28. Cario, L.; Palvadeau, P.; Lafond, A. Mixed-valence state of europium in the misfit layer compound (EuS)<sub>1.173</sub>NbS<sub>2</sub>. *Chem. Mater.* **2003**, *15*, 943–950. [[CrossRef](#)]
29. Liu, B.; Wan, Z.; Zhan, Y. Desulfurization of hot coal gas over high-surface-area LaMeO<sub>x</sub>/MCM-41 sorbents. *Fuel* **2012**, *98*, 95–102. [[CrossRef](#)]
30. Kabongo, G.L.; Mhlongo, G.H.; Mothudi, B.M.; Hillie, K.T.; Mbule, P.S.; Dhlamini, M.S. Structural, photoluminescence and XPS properties of Tm<sup>3+</sup> ions in ZnO nanostructures. *J. Lumin.* **2017**, *187*, 141–153. [[CrossRef](#)]
31. Yu, L.; Diao, G.; Ye, F.; Sun, M.; Zhou, J.; Li, Y.; Liu, Y. Promoting Effect of Ce in Ce/OMS-2 Catalyst for Catalytic Combustion of Dimethyl Ether. *Catal. Lett.* **2011**, *141*, 111–119. [[CrossRef](#)]
32. Setvin, M.; Aschauer, U.; Scheiber, P.; Li, Y.F.; Hou, W.; Schmid, M.; Selloni, A.; Diebold, U. Reaction of O<sub>2</sub> with subsurface oxygen vacancies on TiO<sub>2</sub> anatase (101). *Science* **2013**, *341*, 988–991. [[CrossRef](#)] [[PubMed](#)]

33. Panov, G.; Dubkov, K.; Starokon, E. Active oxygen in selective oxidation catalysis. *Catal. Today* **2006**, *117*, 148–155. [[CrossRef](#)]
34. Oliveira, L.C.A.; Rios, R.V.R.A.; Fabris, J.D.; Sapag, K.; Garg, V.K.; Lago, R.M. Clay–iron oxide magnetic composites for the adsorption of contaminants in water. *Appl. Clay Sci.* **2003**, *22*, 169–177. [[CrossRef](#)]
35. Ferrandon, M.; Carnö, J.; Järås, S.; Björnbom, E. Total oxidation catalysts based on manganese or copper oxides and platinum or palladium I: Characterisation. *Appl. Catal. A* **1999**, *180*, 141–151. [[CrossRef](#)]
36. Topsoe, N.Y.; Topsoe, H.; Dumesic, J.A. Vanadia/Titania Catalysts for Selective Catalytic Reduction SCR of Nitric-Oxide by Ammonia I. Combined Temperature-Programmed in-Situ FTIR and On-line Mass-Spectroscopy Studies. *J. Catal.* **1995**, *151*, 226–240. [[CrossRef](#)]
37. Roy, S.; Viswanath, B.; Hegde, M.S.; Madras, G. Low-Temperature Selective Catalytic Reduction of NO with NH<sub>3</sub> over Ti<sub>0.9</sub>M<sub>0.1</sub>O<sub>2-δ</sub> (M = Cr, Mn, Fe, Co, Cu). *J. Phys. Chem. C* **2008**, *112*, 6002–6012. [[CrossRef](#)]
38. Peña, D.A.; Uphade, B.S.; Smirniotis, P.G. TiO<sub>2</sub>-supported metal oxide catalysts for low-temperature selective catalytic reduction of NO with NH<sub>3</sub>. I. Evaluation and characterization of first row transition metals. *J. Catal.* **2004**, *221*, 421–431.
39. Ye, Q.; Zhao, J.; Huo, F.; Wang, D.; Cheng, S.; Kang, T.; Dai, H. Nanosized Au supported on three-dimensionally ordered mesoporous β-MnO<sub>2</sub>: Highly active catalysts for the low-temperature oxidation of carbon monoxide, benzene, and toluene. *Micropor. Mesopor. Mat.* **2013**, *172*, 20–29. [[CrossRef](#)]
40. Li, H.; Zhang, N.; Chen, P.; Luo, M.; Lu, J. High surface area Au/CeO<sub>2</sub> catalysts for low temperature formaldehyde oxidation. *Appl. Catal. B* **2011**, *110*, 279–285. [[CrossRef](#)]
41. Jiang, X.; Li, X.; Wang, J.; Long, D.; Ling, L.; Qiao, W. Three-dimensional Mn-Cu-Ce ternary mixed oxide networks prepared by polymer-assisted deposition for HCHO catalytic oxidation. *Catal. Sci. Technol.* **2018**, *8*, 274–2749. [[CrossRef](#)]
42. Pang, G.; Wang, D.; Zhang, Y.; Ma, C.; Hao, Z. Catalytic activities and mechanism of formaldehyde oxidation over gold supported on MnO<sub>2</sub> microsphere catalysts at room temperature. *Front. Environ. Sci. Eng.* **2016**, *10*, 447–457. [[CrossRef](#)]
43. Xu, Z.; Yu, J.; Jaroniec, M. Efficient catalytic removal of formaldehyde at room temperature using AlOOH nanoflakes with deposited Pt. *Appl. Catal. B* **2015**, *163*, 306–312. [[CrossRef](#)]
44. Shi, C.; Chen, B.; Li, X.; Crocker, M.; Wang, Y.; Zhu, A. Catalytic formaldehyde removal by “storage-oxidation” cycling process over supported silver catalysts. *Chem. Eng. J.* **2012**, *200*, 729–737. [[CrossRef](#)]
45. Chen, M.; Lin, Y.; Lin, Y.; Lin, H.; Lin, J. Dissociative adsorption of HCOOH, CHOH, and CHO on MCM-41. *J. Catal.* **2004**, *228*, 259–263. [[CrossRef](#)]
46. Chen, B.; Zhu, X.; Crocker, M.; Wang, Y.; Shi, C. FeO<sub>x</sub>-supported gold catalysts for catalytic removal of formaldehyde at room temperature. *Appl. Catal. B* **2014**, *154*, 73–81. [[CrossRef](#)]
47. Zhu, L.; Wang, J.; Rong, S.; Wang, H.; Zhang, P. Cerium modified birnessite-type MnO<sub>2</sub> for gaseous formaldehyde oxidation at low temperature. *Appl. Catal. B* **2017**, *211*, 212–221. [[CrossRef](#)]

